Construction and Building Materials 458 (2025) 139444

Contents lists available at ScienceDirect

Construction and Building Materials

journal homepage: www.elsevier.com/locate/conbuildmat

Flexural performance of RC beams strengthened with HB CFRP plates: Experimental study and theoretical model based on the intermediate crack debonding

A. Codina [a,*], L. Torres [a], T. D'Antino [b], M. Baena [a], C. Barris [a]

[a] AMADE, Polytechnic School, University of Girona, Girona 17003, Spain
[b] Politecnico di Milano, Department of Architecture, Built Environment and Construction Engineering, Milan 20133, Italy

ARTICLE INFO

Keywords:
CFRP strengthening
Debonding
Hybrid bonded FRP
Anchors
Flexural performance
Concrete
Numerical model

ABSTRACT

This paper presents a study on the flexural performance of Reinforced Concrete (RC) beams strengthened with Hybrid Bonded (HB) Carbon Fibre Reinforced Polymer (CFRP) laminates. Single-shear tests and flexural tests on RC beams strengthened with CFRP are examined, comparing both Externally Bonded (EB) and HB strengthening techniques with different anchor spacings. Results show that hybrid bonding improved the bond and flexural capacity in single shear and beam tests, respectively. A numerical model is developed to predict Intermediate Crack Debonding (ICD) in RC beams strengthened with HB CFRP laminates. The methodology is based on considering two different bond-slip laws, one for the EB and another for the HB CFRP portions. The proposed model is validated applying the bond-slip laws calibrated from the EB and HB CFRP single-shear tests to the flexural test results, demonstrating accurate prediction of ICD failure for both EB and HB CFRP specimens.

1. Introduction

In the last decades, there has been a growing acceptance on the use of Fibre Reinforced Polymer (FRP) composites as strengthening solution for existing reinforced concrete (RC) structures due to their several advantages over traditional materials [1]. The Externally Bonded (EB) reinforcement technique is widely used to effectively improve the RC structural performance in terms of bending, shear, torsion, and axial capacity [1,2]. However, existing literature experiments often observed a premature failure in flexural applications due to composite Intermediate Crack Debonding (ICD), originated at an intermediate section of the beam due to flexural or flexural-shear cracks and propagating towards the support [3,4]. This led to a severe underutilization of the FRP material properties. In order to account for ICD, current design guidelines [5–7] have adopted various analytical models involving different levels of approximation. Reviews assessing some formulations in the literature revealed that design models accurately predict ICD failure. However, their reliance on the direct calibration of empirical expressions against experimental results makes them sensitive to variation in certain parameters, such as the fracture energy of the interface where debonding occurs [8].

Various anchorage methods, such as mechanically fastened (MF) metallic anchors, FRP anchors, hybrid anchors, Π-anchors, and U-jacket anchors, have been investigated to enhance the efficacy of FRP strengthening by delaying debonding failure [9,10]. A promising approach, named hybrid bonded (HB)-FRP, has emerged from the combination of MF and EB-FRP, demonstrating effectiveness in providing additional resistance against debonding and contributing to the load-carrying capacity of the RC beams [11]. In this strengthening technique, a sequence of metallic plates is installed on top of the EB-FRP reinforcement and fastened to the concrete substrate. This method offers an advantage over alternative anchorage systems by using the torque applied to the fasteners to enhance frictional resistance [12].

Research efforts have been directed towards the development of methods for predicting the bonding capacity of HB joints. Several studies have investigated factors influencing the bond capacity, such as the bonded length, the number of anchors [13,14], and the exerted pressure on the fasteners [15]. These studies have led to the development of analytical [12,14,16] and numerical [13,17] models aimed at estimating the bond capacity of the joint. Zhang et al. [17] conducted a numerical analysis of the single-shear tests carried out by Gao et al. [13], applying different bond-slip laws to each strengthening system. This

* Corresponding author.
E-mail addresses: alba.codina@udg.edu (A. Codina), lluis.torres@udg.edu (L. Torres), tommaso.dantino@polimi.it (T. D'Antino), marta.baena@udg.edu (M. Baena), cristina.barris@udg.edu (C. Barris).

https://doi.org/10.1016/j.conbuildmat.2024.139444
Received 4 April 2024; Received in revised form 24 October 2024; Accepted 30 November 2024
Available online 13 December 2024

methodology allows the prediction of the bond capacity of HB single-shear specimens. The bond-slip laws derived from [13] were integrated into the numerical model, yielding to good correlation between the experimental data on the single-shear tests and the outcomes of the numerical simulations.

However, design methods providing load limits directly developed from single-shear test configurations are not suitable for predicting ICD in RC beams due to the presence of pulling forces at both ends of the FRP between flexural cracks, instead of just one, as in the case of single-shear tests. In the studies conducted by Teng et al. [18] and Chen et al. [19], an analytical model was developed to investigate the behaviour of an FRP-concrete element subjected to pulling forces at both sides. Nevertheless, the analytical model proposed yielded closed-form equations that are not suitable for including different bond-slip laws in the same specimen, which is the case of the HB system.

Few models have been developed to predict the flexural behaviour of HB-FRP-strengthened RC beams, including analytical [20], Finite Element Method (FEM) [21,22] and simplified bond strength models [20,22–25]. Analytical models provide a simple description of the phenomena, but they do not allow for changes in the bond-slip laws, which may be necessary with further research into HB-FRP joint behaviour. In contrast, FEM models offer the advantage of allowing the introduction of different bond-slip laws at each location, although their complexity can be a potential drawback. Simplified bond strength models, on the other hand, present a concise approach using few equations that consider both the adhesive bond contribution of the EB reinforcement and the frictional contribution of the anchor. However, these models rely on empirical coefficients calibrated with a limited number of tests, potentially reducing accuracy in predictions when altering parameters.

In this study, the results of an experimental campaign based on single-shear tests and RC beams strengthened with EB and HB-CFRP pultruded laminates are presented. The effectiveness of HB-FRP method in delaying debonding failure is analysed both in single-shear and flexural configurations. Experimental results are presented and discussed in terms of modes of failure, bond and flexural capacity for single-shear tests and beams, respectively, load-displacement response, and load-strain response in the CFRP. A numerical methodology for predicting ICD applicable to RC beams strengthened with FRP reinforcement is presented. The proposed model can be applied to any type strengthening technique, provided that the bond-slip law of the interface between external reinforcement system and concrete is known. The experimental results from single-shear tests are used to obtain the bond-slip law of the CFRP-concrete joints, which is then used to validate the model with the experimental results from flexural tests.

2. Experimental programme

The experimental programme comprised single-shear tests and beam flexural tests. The single-shear tests were used to characterise the bond-slip laws of the CFRP-concrete joint for the applied strengthening configurations (i.e., EB and HB) that were subsequently used for the calculation of the ICD failure loads of the beams. The main parameters of the programme were the strengthening technique (EB and HB) and, specifically in HB beam tests, the anchor spacing. Fig. 1 shows the anchor used in HB specimens.

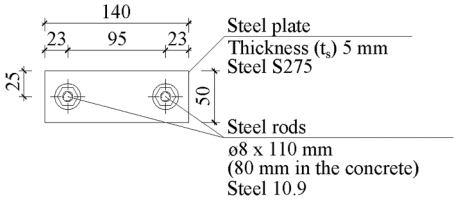

Fig. 1. Anchor details (dimensions in mm).

Six concrete blocks and three beam specimens were cast from the same concrete batch. The concrete average compressive strength (f_{cm}), tensile strength (f_{ctm}) and modulus of elasticity (E_c) were determined from three cylinder tests of 150 mm diameter and 300 mm high according to UNE-EN 12390-3 [26], UNE-EN 12390-6 [27] and ASTM C469/C469M-10 [28] standards, obtaining 45.98 MPa (with a Coefficient of Variation, CoV=5.59 %), 3.94 MPa (CoV=2.93 %), and 36.21 GPa (CoV=0.60 %).

The mechanical properties of the steel bars used for internal reinforcement were determined from tensile tests according to UNE-EN ISO 15630-1 [29], which provided an average yielding strength (f_y), yielding strain (ε_y) and modulus of elasticity (E_s) of 569.96 MPa (CoV=2.18 %), 0.27 % (CoV=0.76 %) and 208.58 GPa (CoV=1.80 %), respectively.

The CFRP pultruded laminates used in this experimental work were the S&P C-Laminates, consisting of unidirectional carbon fibres with a fibre volume fraction higher than 68 %, 50 mm width (b_f), and 1.4 mm thickness (t_f). The mechanical properties provided by the manufacturer (S&P) were a tensile strength (f_{fu}) of 2800 MPa, a tensile strain (ε_{fu}) of 1.60 % and a modulus of elasticity (E_f) of 170 GPa.

The two-component epoxy resin used to bond the CFRP laminates was the thixotropic, solvent-free adhesive, S&P Resin 220 HP with a density of approximately $1.6{\cdot}10^3$ kg/m^3. The tensile strength of this epoxy resin was 15 MPa and the modulus of elasticity is 7.10 GPa, after a curing time of 7 days, according to the manufacturer data sheet.

For the EB technique, surface preparation involved the removal of the weak outer layer of concrete through bush-hammering [30], followed by cleaning with compressed air. Besides, in the HB technique, holes of 10 mm diameter and 80 mm depth were drilled into the concrete and cleaned with compressed air. The holes were then filled with the polyester hybrid mortar Fischer FIS P Plus 300 T, and the steel threaded rods were immediately placed inside the holes. In both techniques, the CFRP laminate was bonded onto the concrete surface by applying a thin layer of epoxy resin. After 24 hours of curing the epoxy resin, S275 structural steel plates (see Fig. 1) were bonded onto CFRP laminates in the HB specimens using the same epoxy resin. One day after bonding the steel plates, washers and nuts were fastened with a torque of 10 Nm. The torque used was selected based on the torque range found in the available literature [15,20,24]. Preliminary test results confirmed that this torque provided a significant contribution to the joint capacity. Before testing, the strengthening system was cured for 11 days at laboratory conditions.

In the following sub-section, the setup and instrumentation of both testing configurations are presented.

2.1. Test setup and instrumentation

2.1.1. Single-shear tests

Six concrete blocks externally strengthened with one CFRP laminate 50 mm wide and 1.4 mm thick were tested under the single-shear test configuration as shown in Fig. 2. The concrete block dimensions were 200 mm × 200 mm × 370 mm. Three different bonding configurations were tested: EB (Fig. 2a), HB in which one anchor was placed in the middle of the EB bonded length (Fig. 2b), and HB in which only the EB part under the anchor (placed in the middle of the EB bonded length) was bonded onto the concrete (Fig. 2c). The bonded length considered is reported in Table 1, specifying the lengths of the non-anchored parts at the loaded and free ends, as well as the anchored length. An EB bonded length of 250 mm was chosen to ensure that it was higher than the effective bonded length computed according to various analytical models [6,7,31,32,33]. A distance of at least 50 mm was left unbonded beyond the laminate loaded end to avoid concentration of stresses in the concrete [34]. The characteristics of the single-shear specimens are reported in Table 1. The specimens were designated as X-Y-A, where X is the strengthening technique (EB or HB), Y is the laminate bonded length (50 or 250 mm) and A indicates the number of the test within the series.

A hydraulic jack pulled the CFRP laminate under displacement-

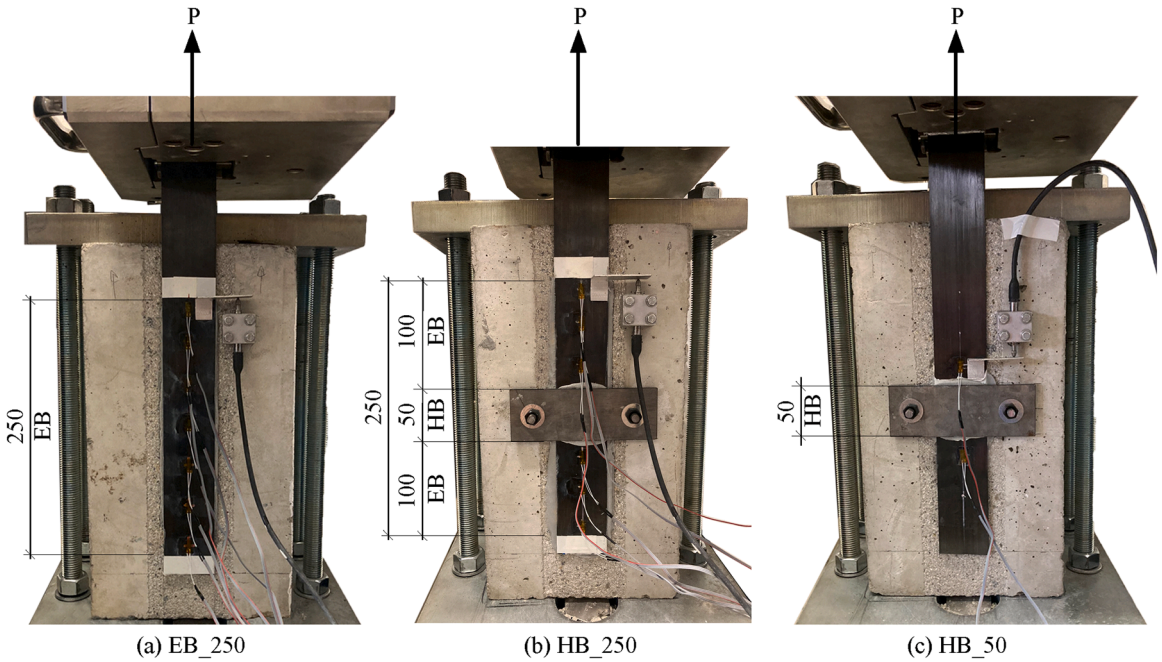

Fig. 2. Single-shear test specimens (a) EB-250, (b) HB-250 and (c) HB-50 (dimensions in mm).

Table 1
Characteristics of the single-shear test specimens.

Specimens			Bonded length		
Label	No	Method	EB from loaded end (mm)	HB (mm)	EB from free end (mm)
EB−250	2	EB	250	-	-
HB−250	2	HB	100	50	100
HB−50	2	HB	-	50	-

controlled conditions at a rate of 0.18 mm/min. The applied load was measured with a 125 kN load cell and one linear variable displacement transducer (LVDT) was used to measure the relative displacement (slip) between the CFRP and the concrete at the loaded end. Strain gauges (SG) were used to acquire the strain profile along the bonded length of the CFRP laminate (Fig. 2), which also allowed the computation of the slip at the loaded end. These values were used to cross-validate the measurements of the LVDT.

2.1.2. Beam tests

Three RC beams externally strengthened with one CFRP laminate 50 mm wide and 1.4 mm thick were tested under a 4-point bending configuration. In two of the specimens, metallic plates were bonded on top of the EB-CFRP laminate with two different spacings (Fig. 3b and c). Specimens had a distance between supports of 2200 mm, a shear span of 900 mm and a cross section of 140 mm width and 180 mm depth (Fig. 3 and Table 2). The ratio between the shear span and effective depth, as well as the length of the CFRP laminate, were chosen to induce failure by ICD [35]. The internal tensile steel reinforcement consisted of two bars of diameter 10 mm, two bars of diameter 6 mm as compression reinforcement, and stirrups of diameter 8 mm placed along the beam length with a spacing of 100 mm. The specimens were designated as X-SY, where X is the strengthening technique (EB or HB) and Y is the anchor spacing, when applicable (100 mm or 300 mm).

A hydraulic jack applied the load at the centre of a spreader beam under displacement-controlled conditions with a rate of 0.60 mm/min. The applied load was measured by a 200 kN load cell. The mid-span deflection was assessed using three LVDTs: one LVDT located at the beam mid-span to monitor the vertical displacement and one at each support to measure possible settlements. The CFRP tensile strain was obtained through three SG attached onto its surface. One SG was placed at the mid-span and one under each load application point to measure the strain in the constant (maximum) bending moment region. The concrete strain was measured using one SG attached at the mid-span top section of the beam.

3. Experimental results and discussion

In this section, the results of single-shear tests are reported in terms of bond capacity, failure modes, and load responses. Then, results of the flexural tests are discussed in terms of load-deflection and load-strain behaviour, failure modes, and crack patterns.

3.1. Single-shear tests

3.1.1. Bond capacity and failure modes

Values of the maximum load (P_{max}) and slip (s_{max}) measured in the single-shear tests are presented in Table 3. A notable increase in the maximum load was observed in the HB specimens compared to the EB. Specifically, the addition of one anchor to the EB specimen with a torque of 10 Nm (i.e., specimen HB-250 with 250 mm of bonded length and the anchor placed in the middle of this length), resulted in a 35 % increase in the average bond capacity, followed by an increment in the maximum slip. In contrast, specimen HB-50, with only 50 mm of anchored bonded length, showed a lower bond capacity, as expected, due to the reduced bonded length. In all cases, failure occurred within a thin weak outer layer of concrete (Fig. 4). This failure mode is consistent with that observed in the EB specimens, indicating that the introduction of anchors did not change the failure interface.

3.1.2. Load-slip behaviour

The applied load-slip curves of the specimens tested are reported in Fig. 5. The EB-250 specimens followed an ascending branch up to approximately 39 kN. Then, the applied load plateaued, confirming that the effective bonded length was achieved, until failure occurred at a slip of approximately 0.50 mm.

The HB-250 specimens, which had the same bonded length as the EB-250, followed the same behaviour of the EB specimens until they

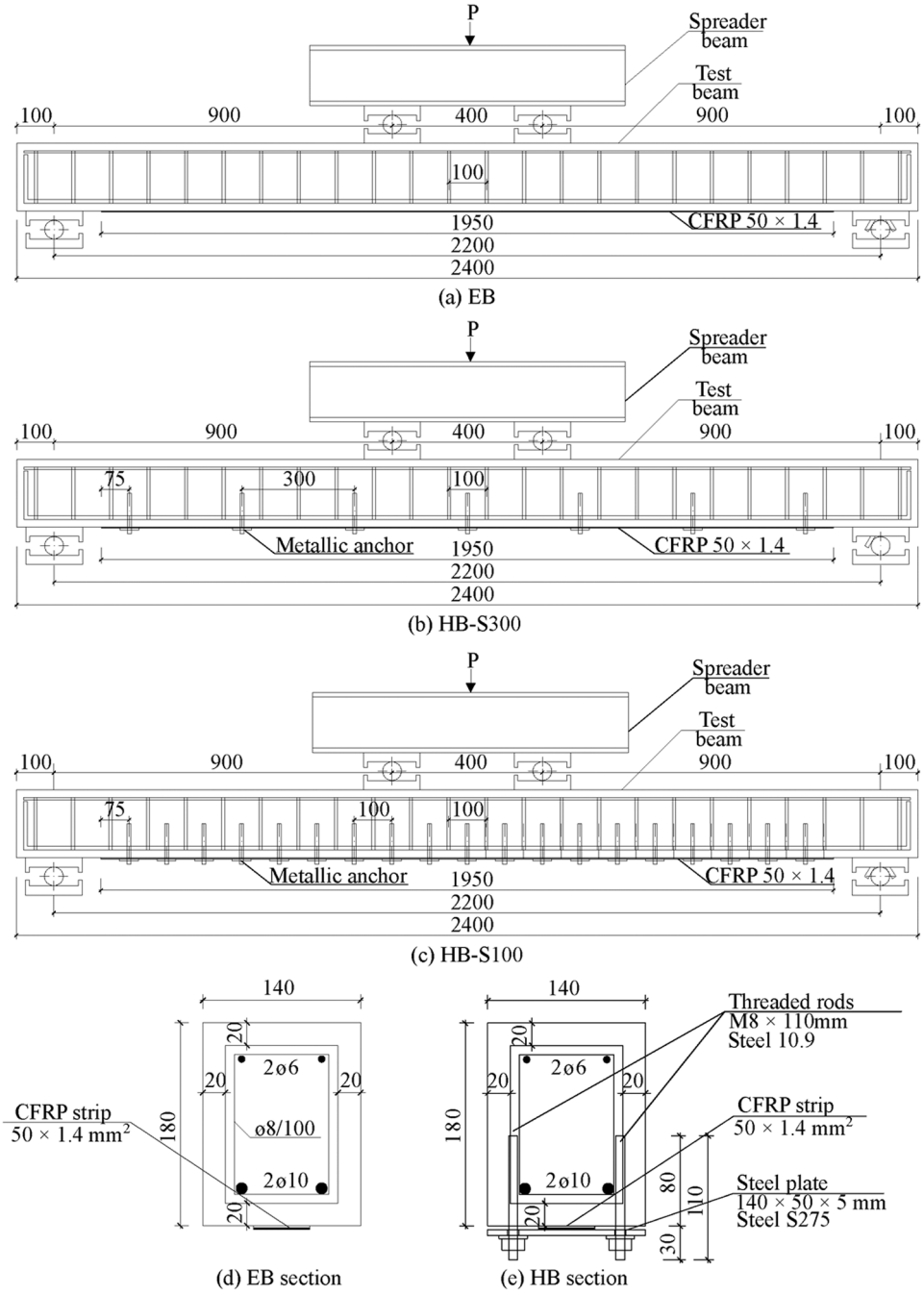

Fig. 3. Beam specimens (dimensions in mm).

Table 2
Geometrical characteristics of the beam test specimens.

Specimens			Anchors		Steel reinforcement	
Label	No	Method	Total No	Spacing (mm)	Compression	Tension (A_{S1})
EB	1	EB	-	-	2ø6	2ø10
HB-S300	1	HB	7	300	2ø6	2ø10
HB-S100	1	HB	19	100	2ø6	2ø10

Table 3
Experimental results of single-shear tests.

Specimen	P_{max} (kN)	Avg. P_{max} (kN)	s_{max} (mm)
EB-250-1	38.02	39.23	0.49
EB-250-2	40.44		0.52
HB-250-1	50.90	52.93	0.66
HB-250-2	54.95		0.70
HB-50-1[1]	28.83	28.83	1.21

[1] Two specimens were tested, however, due to problems in the data acquisition system, one of the tested specimens was excluded from the analysis.

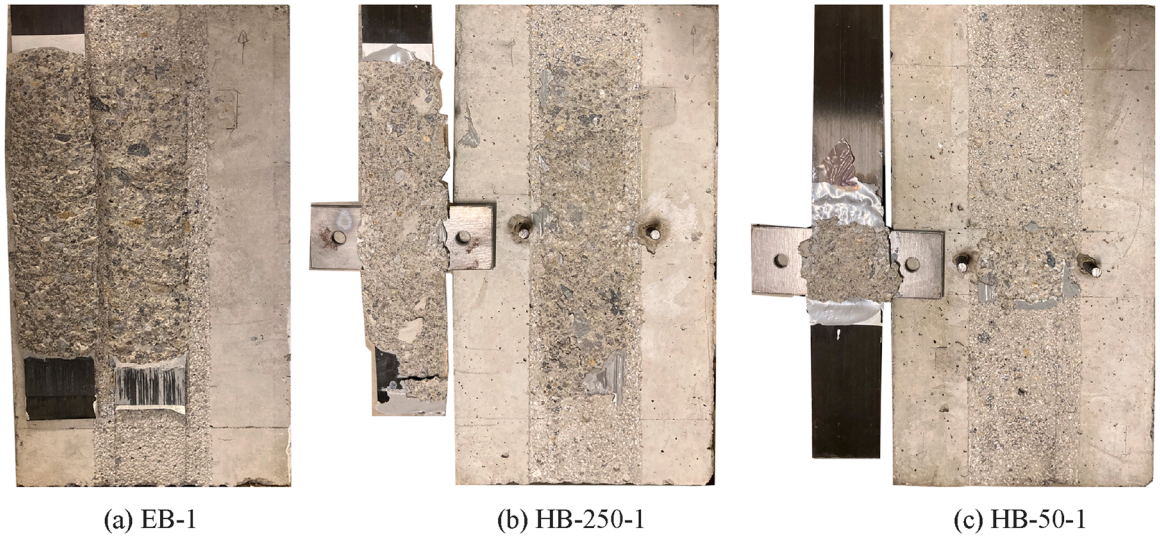

Fig. 4. Debonding failure modes of single-shear tests.

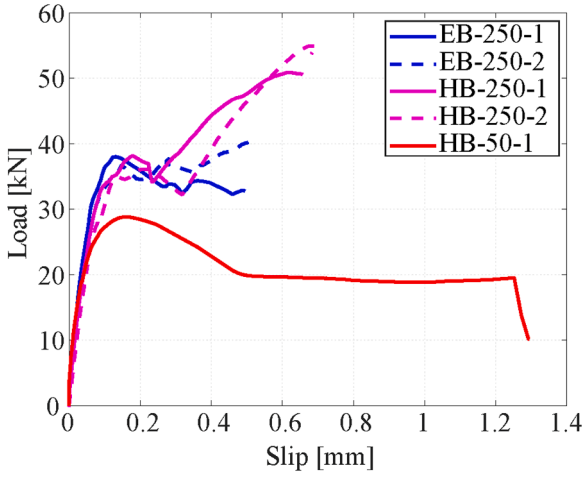

Fig. 5. Experimental load-slip curves of single-shear tests.

reached a slip value of 0.20 mm and 0.30 mm, depending on the specimen (see Fig. 5). In this phase, where the plateau was developed, debonding of the portion of CFRP laminate between the anchor and the loaded end was observed. After the plateau, the load kept increasing until sudden failure due to complete debonding of the CFRP laminate occurred.

The HB-50 specimen followed the same initial behaviour as the other specimens. However, due to a shorter bonded length with respect to other specimens, the initial branch only increased up to an applied load value of 29 kN. After that, since the bonded length was smaller than the effective bonded length, the load-slip curve followed a descending path until it reached a load of 20 kN. Finally, the curve followed a horizontal branch attributed to the friction provided by the anchor.

3.2. Beam tests

3.2.1. Flexural capacity and failure modes

Table 4 presents the maximum applied load (P_{max}), maximum mid-span deflection (δ_{max}), maximum CFRP strain ($\varepsilon_{f,max}$), maximum concrete strain ($\varepsilon_{c,max}$), and failure mode obtained by the beam tests. The bending capacity increased ($\Delta P_{\max,EB}$) in HB specimens compared to EB. With an anchor spacing of 300 mm, there was a delay in the ICD failure mode, resulting in an 8 % enhancement in load-carrying capacity. Nevertheless, reducing the anchor spacing to 100 mm completely prevented debonding, causing failure by concrete crushing (CC) at the mid-span cross section top and leading to a 27 % increase in maximum applied load compared to the EB. Moreover, HB technique led to a more efficient use of the CFRP laminate, which could attain higher strain values, which increased from approximately 0.63–0.74 % in specimen HB-S300 and to 1.23 % in specimen HB-S100.

Regarding the failure modes, in the EB specimen, the laminate suffered ICD, detaching from the surface along with the weak outer layer of concrete (Fig. 6a). While precisely identifying the exact initiation point of debonding is challenging, the widest and deepest cracks were observed far from the end anchorage region and near the load application locations.

From visual inspection of specimen HB-S300, it was observed that the laminate only detached in specific areas near the load application points, as illustrated in Fig. 6c. The anchors effectively retained the remaining portion of the laminate attached to the surface.

In the case of specimen HB-S100, localised debonding was also observed (Fig. 6d). Nevertheless, anchors succeeded in maintaining the laminate attached to the beam until failure by CC occurred (Fig. 6b).

Table 4
Experimental results of beam tests.[1]

Specimen label	P_{max} (kN)	$\Delta P_{\max,EB}$ (%)	δ_{max} (mm)	$\varepsilon_{f,max}$ (%)	$\Delta\varepsilon_{f,max,EB}$ (%)	$\varepsilon_{c,max}$ (%)	$\Delta\varepsilon_{c,max,EB}$ (%)	Failure mode
EB	53.23	-	24.36	0.63	-	−0.16	-	ICD
HB-S300	57.68	8	58.57	0.74	17	−0.21	31	ICD
HB-S100	67.77	27	44.54	1.23	95	−0.30	88	CC

[1] where P_{max} = maximum applied load, δ_{max} = maximum mid-span deflection, $\varepsilon_{f,max}$ = maximum CFRP strain, $\varepsilon_{c,max}$ = maximum concrete strain, and $\Delta P_{\max,EB}$, $\Delta\varepsilon_{f,max,EB}$, $\Delta\varepsilon_{c,max,EB}$ = increase of HB compared to EB in load-carrying capacity, maximum CFRP strain, and maximum concrete strain, respectively. ICD = intermediate crack debonding, CC = concrete crushing.

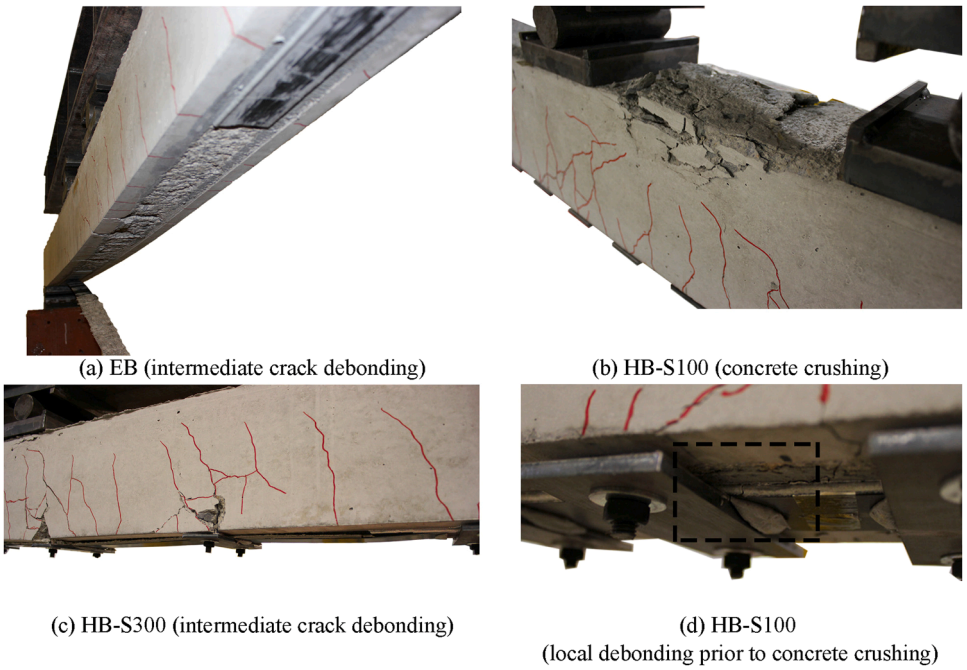

Fig. 6. Failure modes of tested beams.

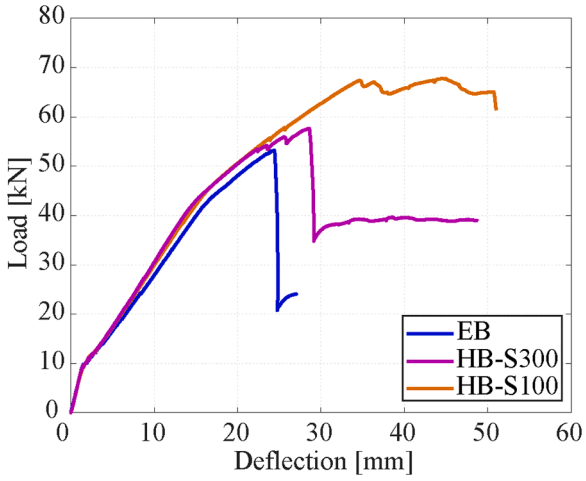

Fig. 7. Experimental load-deflection curves of tested beams.

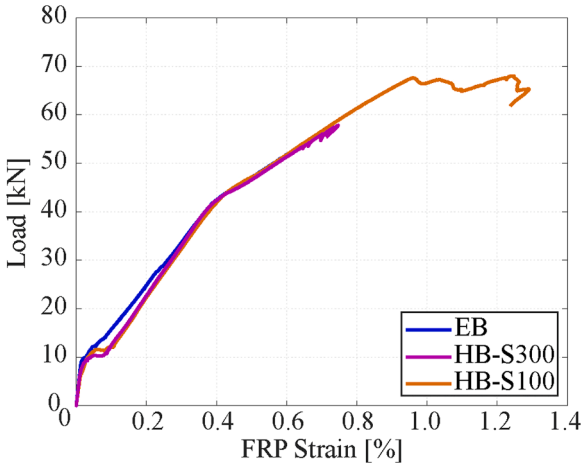

Fig. 8. Experimental load-strain curves for beams.

3.2.2. *Load-deflection and load-strain behaviour*

Experimental load versus mid-span deflection curves are represented in Fig. 7. The load-deflection curves of HB specimens were slightly stiffer than EB specimen after the cracking load, probably due to the improvement of bond between CFRP and concrete, and presented a higher peak load value. Additionally, HB-S100 displayed a significant increase compared to HB-S300 in terms of load-carrying capacity.

Both EB and HB-S300 beams exhibited local debonding at approximately 53 kN, represented by drops in the load-deflection curves (Fig. 7). While the EB technique failed to prevent the debonding propagation towards the supports, resulting in beam failure, the anchors in specimen HB-S300 could retain the laminate attached to the concrete surface. This allowed for an increase in load, although the beam eventually reached failure due to debonding. In the case of specimen HB-S100, the first local debonding occurred at 56 kN, slightly higher than in the other beams. Nevertheless, the closer anchor spacing successfully prevented the propagation of debonding.

Experimental load versus CFRP strain curves at the beam mid-span are represented in Fig. 8. A similar behaviour was observed in the load-strain curves of the different specimens, with variation in the maximum values at failure only. The difference in the strain value associated with the cracking moment at approximately 10 kN was due to the different positions of the cracks with respect to that of the strain gauges.

3.2.3. *Crack patterns*

Fig. 9 displays the crack patterns of the tested specimens at failure, with the indication of the load point positions. The minimum ($s_{r,min}$), maximum ($s_{r,max}$), and average ($s_{r,avg}$) experimental crack spacings are detailed in Table 5, alongside the predicted crack spacing at the ultimate limit state (ULS) ($s_{r,th}$) according to the model presented in [36]. This prediction model proposes the formulation in Eq. (1) to (6), where $l_{e,0}$ represents the transfer length of the reinforcing steel, M_{cr} is the cracking moment, z_s is the steel lever arm (approximated to 0,85 h), $W_{c,0}$ is the section modulus of the uncracked concrete gross section, F_{bsm} is the bond force per unit length, $n_{s,i}$ is the number of steel rebars with diameter $\phi_{s,i}$, f_{bsm} is the mean bond stress, and the parameters $\kappa_{\iota b1}$ and

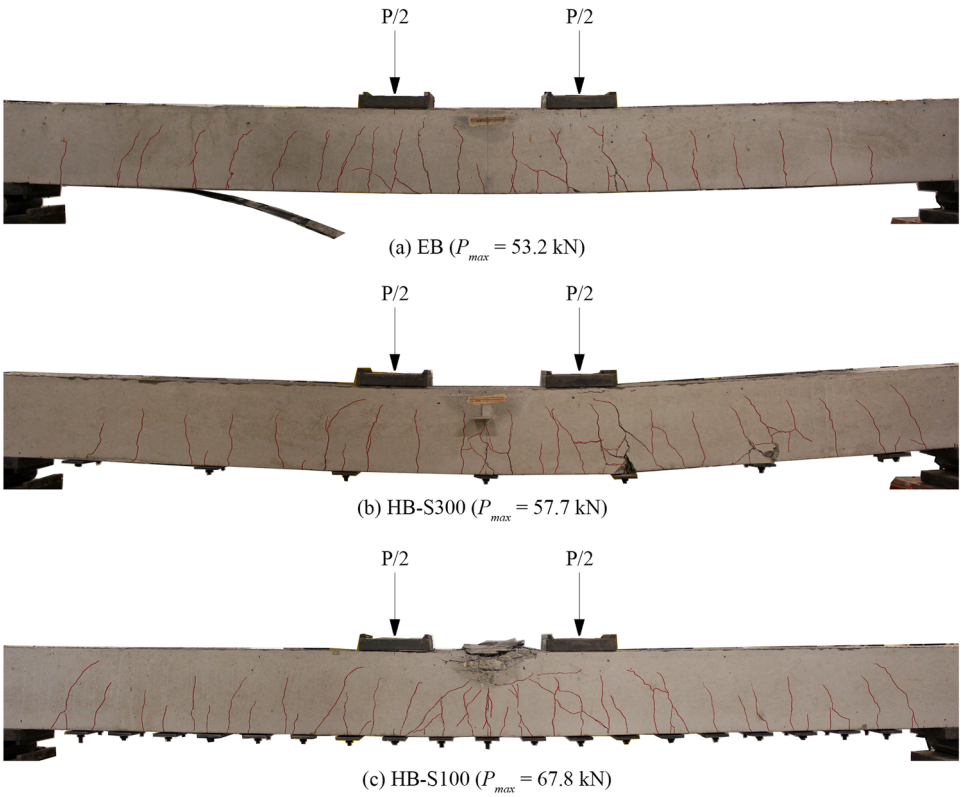

Fig. 9. Beam experimental crack patterns at ultimate load.

Table 5
Experimental and theoretical values of crack spacing at ultimate load.[1] CoV (%) of the average values is reported in parenthesis.

Specimen label	*no of cracks* (-)	$s_{r,min}$ (mm)	$s_{r,max}$ (mm)	$s_{r,avg}$ (mm)	$s_{r,th}$ (mm)	$s_{r,th}$ /$s_{r,avg}$ (dimensionless)
EB	30	18	140	68 (50)	120	1.76
HB-S300	33	13	136	59 (57)	120	2.01
HB-S100	44	7	117	46 (52)	120	2.62

[1] where $s_{r,min}$, $s_{r,max}$, $s_{r,avg}$ are the minimum, maximum and average experimental crack spacings, and $s_{r,th}$ is the predicted crack spacing at the ULS according to Ref. [36].

κ_{lb2} can be assumed equal to 1.0 for good bond conditions and $\kappa_{lb1} = 0.7$ and $\kappa_{lb2} = 0.5$ for medium bond conditions.

$$s_r = 1.5 l_{e,0} \tag{1}$$

$$l_{e,0} = \frac{M_{cr}}{z_s \cdot F_{bsm}} \tag{2}$$

$$M_{cr} = \kappa_{fl} \cdot f_{ctm} \cdot W_{c,0} \tag{3}$$

$$\kappa_{fl} = \left(1.6 - \frac{h}{1000}\right) \geq 1 \tag{4}$$

$$F_{bsm} = \sum_{i=1}^{n} n_{s,i} \pi \cdot \varnothing_{s,i} \cdot f_{bsm} \tag{5}$$

$$f_{bsm} = \begin{cases} 0.43 \kappa_{lb1} \cdot f_{cm}^{2/3} & \text{for ribbed bars} \\ 0.28 \kappa_{lb2} \cdot \sqrt{f_{cm}} & \text{for smooth bars} \end{cases} \tag{6}$$

In all cases, closer cracks were found in the constant bending moment region, while higher crack spacings were observed near the supports. Moreover, the introduction of anchors contributed to narrower crack spacings around them, resulting in a less uniform crack distribution. As the anchor spacing decreased, the values of minimum, maximum and average crack spacings also decreased. Fig. 9 illustrates this phenomenon, showing that there is at least one crack near each anchor, either in the middle or the sides.

Upon comparing experimental values with theoretical predictions ($s_{r,th}$), it is observed that the latter are consistently higher, with the difference becoming more obvious as the spacing between anchors reduces.

4. Calibration of bond-slip law parameters

To obtain the parameters of the bond-slip law, a numerical procedure based on the finite differences method [37] was used considering the load-slip curves obtained in the single-shear tests. The model is specifically designed to solve the governing equation of the bonded joint, allowing the use of various types of local bond-slip relationships. Within this methodology, the overall bonded length (L) is subdivided into equally spaced segments of length $\Delta x = L/n$ (Fig. 10), where n denotes the total number of divisions. Employing an incremental slip method, the adopted approach effectively simulates the debonding process.

Starting from the loaded end and progressing towards the free end,

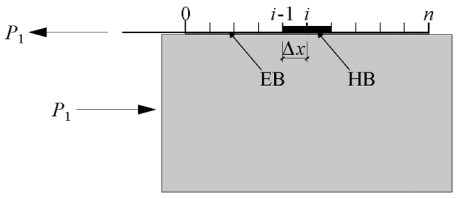

Fig. 10. Discretization of the single-shear specimen for the finite difference numerical model.

the procedure calculates the slip and load transfer between adjacent sections for each analysed point. At a given slip value at the loaded end, an iterative process is executed. The applied load P_1 (see Fig. 10) is utilized to determine the corresponding strains in the FRP (ε_f), concrete (ε_c), and the bond-shear stress (τ) using the corresponding bond-slip law for each strengthening technique (EB and HB) at the loaded end. At iteration j, the load, $P(j,i)$, and slip, $s(j,i)$, at each point i are computed using Eqs. (7) and (8), respectively, along the FRP.

$$P(j,i) = P(j,i-1) - \tau(j,i-1)\cdot L_{per}\cdot\Delta x \tag{7}$$

$$s(j,i) = s(j,i-1) - \left(\varepsilon_f - \varepsilon_c\right)\cdot\Delta x \tag{8}$$

where L_{per} is the bonded perimeter between FRP and concrete. A nominal perimeter length equal to the CFRP laminate width was considered in all cases, for both EB and HB. Increments of P_1 are applied at the loaded end until the FRP strain at the free end ($\varepsilon_{f,n}$) reaches the specified boundary condition $\varepsilon_{f,threshold}$. This threshold is set to be a value close to zero. This iterative procedure is repeated for each increment of slip at the loaded end until failure occurs.

Based on different models available in the literature [12–14,22,38], bilinear and trilinear bond-slip laws were selected in this study to assess the experimental bond behaviour of the EB and HB joints, respectively (Fig. 11a). An inverse analysis, using a least-squares approach, was conducted to identify the bond-slip parameters that best fitted the experimental load-slip curves [37,39], and the results obtained are reported in Table 6. Initially, the calibration of the EB bond-slip law was performed considering results of specimen EB-250. Then, the parameters of the HB technique were calibrated using specimen HB-50. Finally, results were applied in specimen HB-250 (Fig. 11b), in which each of the two previous bond-slip laws was implemented in the proper position. The calibrated parameters include the shear stress (τ_f) and the corresponding slip (s) at the end of the three stages of the bond-slip behaviour (Fig. 11a): $\tau_{f,1}$ and s_1 for the linear elastic stage (0–1 in Fig. 11a), $\tau_{f,2}$ and s_2 for the linear softening stage of the EB specimen (1–2 in Fig. 11a), and $\tau_{f,3}$ and s_3 for the linear softening stage of the HB specimen (2–3 in Fig. 11a), which correspond with the initiation point of the residual branch with constant stress (point 3 in Fig. 11a). The bond-slip relationships and the comparison between theoretical and experimental load-slip curves are represented in Fig. 11a and b, respectively.

Analysing the results of the single-shear tests, it can be noted that the addition of the anchor did not modify the bond-slip behaviour of the EB but introduces a supplementary contribution that entails for the presence of friction (anchor contribution in Fig. 11a). Upon initiation of micro-cracking in the FRP-concrete interface, the anchor starts to contribute, marking the onset of an initial linear ascending phase until the initiation of debonding in the EB. Subsequently, the anchor contribution gradually diminishes until complete HB debonding occurs, at which point it stabilizes to a constant value due to friction.

Table 6
Bond-slip law parameters calibrated from the experimental load-slip curves.

Specimen	$\tau_{f,1}$ (MPa)	s_1 (mm)	$\tau_{f,2}$ (mm)	s_2 (mm)	$\tau_{f,3}$ (mm)	s_3 (mm)
EB	12.70	0.03	-	0.18	-	-
HB	12.70	0.03	10.70	0.18	7.40	0.42
Anchor	-	0.03	10.70	0.18	7.40	0.42

5. Proposed model for the assessment of the ICD failure in beams strengthened with HB-CFRP

5.1. Model description

The study focuses on the failure mode by ICD, where the FRP laminate in a strengthened concrete element between cracks is subjected to tension at both sides (Fig. 12a), which provides a bond scenario different from that of the single-shear test. To address this, the beam is discretized in different elements between cracks, and the bonded joint model previously used for the single-shear test (Fig. 10) is adjusted by introducing an additional pulling force at the end of the FRP laminate previously free (Fig. 12b). This model was formerly introduced in a preceding research paper by the authors and was successfully applied to the Externally Bonded Reinforcement on Grooves (EBROG) system [40]. In Ref. [40], the same bond-slip law was implemented along the joint. However, for the HB-FRP technique, the calibrated bond-slip laws of EB and HB specimens are assigned to their corresponding Δx portions. Equilibrium Eqs. (9) and (10) establish the relationship between the forces at a cracked section, including concrete, steel, and FRP forces. The coefficient α, within the range of $0 < \alpha < 1$, represents the ratio between the pulling forces in the higher (crack 1 in Fig. 12a) and lower (crack 2 in Fig. 12a) loaded ends. Consequently, it will also relate the values of the FRP laminate strain at both ends, modifying the boundary condition $\varepsilon_{f,threshold}$ in Eq. (11).

$$F_{f1} = F_{s1} - F_{c1} = P_1 \tag{9}$$

$$F_{f2} = F_{s2} - F_{c2} = \alpha P_1 \tag{10}$$

$$\varepsilon_{f,threshold} = \varepsilon_{f,n} = \alpha\cdot\varepsilon_{f,0} \tag{11}$$

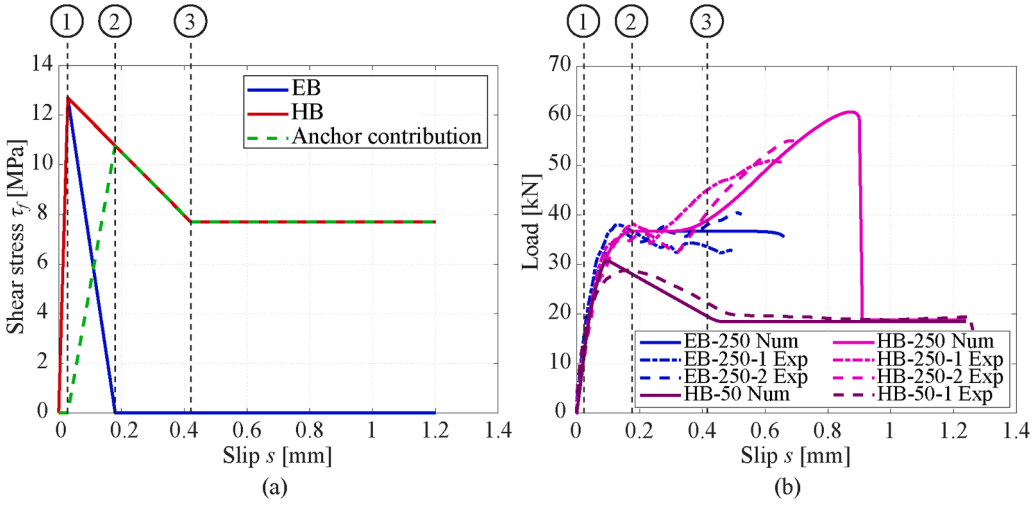

Fig. 11. Bond-slip relationships identified for the tested specimens.

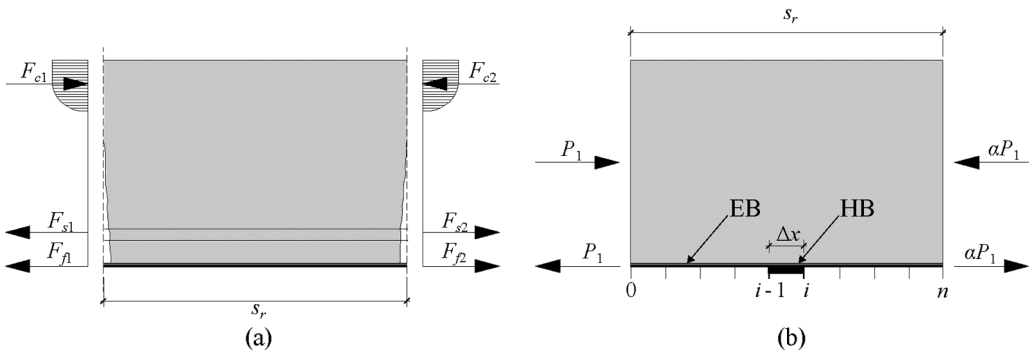

Fig. 12. (a) Forces in the beam concrete element between cracks and (b) bonded joint model for predicting ICD.

5.2. Assessment of the influence of anchor position on the bond capacity in the element between cracks

Given a bond-slip law for each strengthening system, the bond capacity calculation for the concrete element between flexural cracks primarily depends on three key parameters: the variation in tensile forces in the FRP at both sides of the element between cracks (α), the bonded length, represented by the crack spacing s_r, and the position of the anchor in the bonded joint. To assess the influence of the anchor position, a parametric study was performed. Maintaining a fixed crack spacing corresponding to the average experimental value in the EB beam ($s_{r,avg}$ in Table 5, equal to 68 mm), three anchor positions were considered (Fig. 13). Given that the numerical model is based on the position of the cracks, these cases aim to recognize significant differences resulting from considering the crack at the midpoint of the anchor (Fig. 13a), or at the higher and lower ends of the plate (Fig. 13b and c, respectively).

The results obtained are illustrated in Fig. 14a for two ratios of pulling forces. The coefficient $\alpha = 0$ corresponds to a single-shear test and $\alpha = 1$ represents the case of symmetrical loads. The value of $\alpha = 0.7$ was selected based on a theoretical estimation of FRP tensile forces around the load application points, where debonding most likely initiated according to visual inspection of the beams [40]. The bond-slip laws calibrated from the single-shear tests (Fig. 11a) were used in this parametric study (Fig. 14b).

5.2.1. Load-slip curves – maximum load and stiffness

The analysis of Fig. 14 reveals that the inclusion of an anchorage (HB) significantly enhances the load capacity of the joint, irrespective of its position, for both $\alpha = 0$ (increase of 20 %, 25 % and 8 % for cases A, B and C, respectively) and $\alpha = 0.7$ (increase of 66 %, 99 % and 73 % for cases A, B and C, respectively). Moreover, it can be observed that the introduction of a balancing force ($\alpha = 0.7$) has a substantial impact on the load capacity of the joint, both for EB (increase of 57 %) and HB (increase of 116 %, 150 % and 150 % for cases A, B and C, respectively).

The load-slip curves demonstrate higher stiffness for the specimens with anchor at the higher loaded end (cases A and B) compared to its placement at the lower loaded end (case C), corresponding to the higher shear stress attained by the HB specimens in the softening part.

5.2.2. Influence of anchor position for $\alpha = 0$

In the case of $\alpha = 0$, the load capacity of the HB joint exhibits a downward trend as the anchor is progressively moved towards the free end. This behaviour occurs due to the difference between the bond-slip laws of EB and HB for high slip values (Fig. 14b), which take place near the loaded end. If the anchor is positioned at the loaded end (cases A and B), the remaining EB portion is subjected to lower load values, enabling it to transfer shear stresses even when the anchor reaches the constant residual strength. Conversely, placing the anchor at the free end (case C), the anchor effect is visible when the EB portion already experienced significant slips, making the EB interface incapable of transferring shear stresses as it undergoes debonding when the anchor attains the constant residual strength.

5.2.3. Influence of anchor position for $\alpha = 0.7$

In the case of $\alpha = 0.7$, the HB specimens still exhibit the highest bond capacity when the full anchor is located at the higher loaded end (case B, 102.2 kN). However, in contrast with the scenario with $\alpha = 0$, placing the full anchor at the lower loaded end results in higher bond capacity (case C, 89.0 kN) than having half anchor at each end (case A, 85.3 kN). This shift in the behaviour is attributable to the compensating force, which now activates the longer anchored length at the lower loaded end when the EB portion already experienced significant slips.

Fig. 15 shows the shear stress distributions at the maximum load (P_{max}, black curves) for each anchor position considered. Curves corresponding to different steps of load are included for comparison. The green curve P_{res} corresponds to the residual load after debonding.

In the HB joint, for case B, after the maximum shear stress has propagated to the lower loaded end of the anchor (black curve, position = 50 mm), the unanchored zone can still develop a significant part of the shear stress profile (position = 50–68 mm), resulting in a larger area under the curve and, consequently, a higher load capacity than cases A and C. For these other two cases, once the maximum shear stress reaches

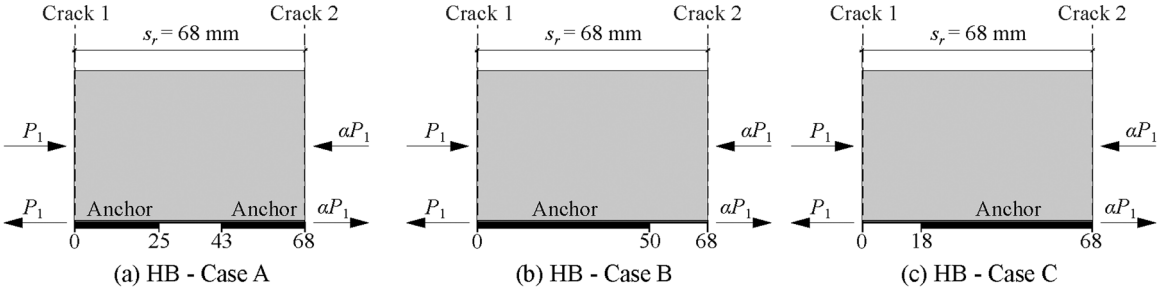

Fig. 13. Studied anchor positions within the bonded joint: (a) one crack at the middle of each anchor (HB-Case A); (b) crack located at the higher loaded anchor end (HB-Case B), and (c) crack located at the lower loaded anchor end (HB-Case C).

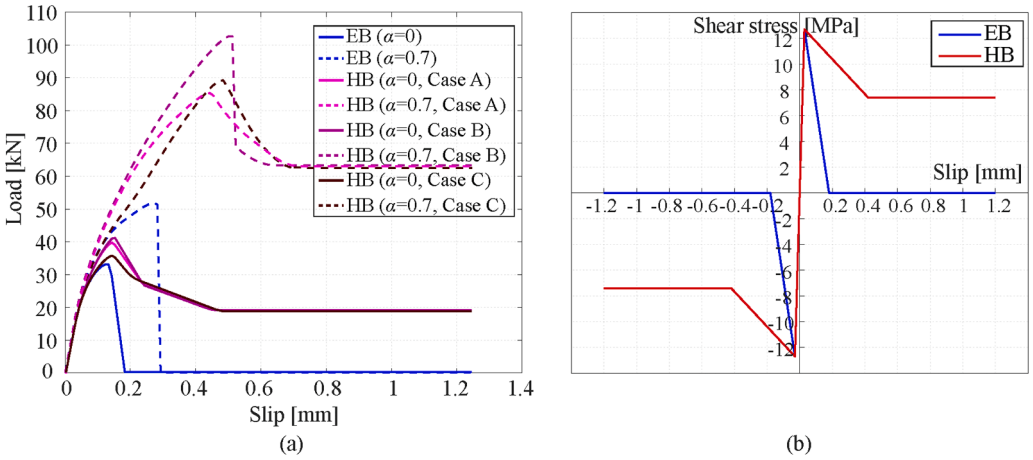

Fig. 14. (a) Load (P_1 in Fig. 12b) versus slip for different ratios (α) between pulling forces in the element between cracks and anchor positions, using the (b) bond-slip laws calibrated from the single-shear tests.

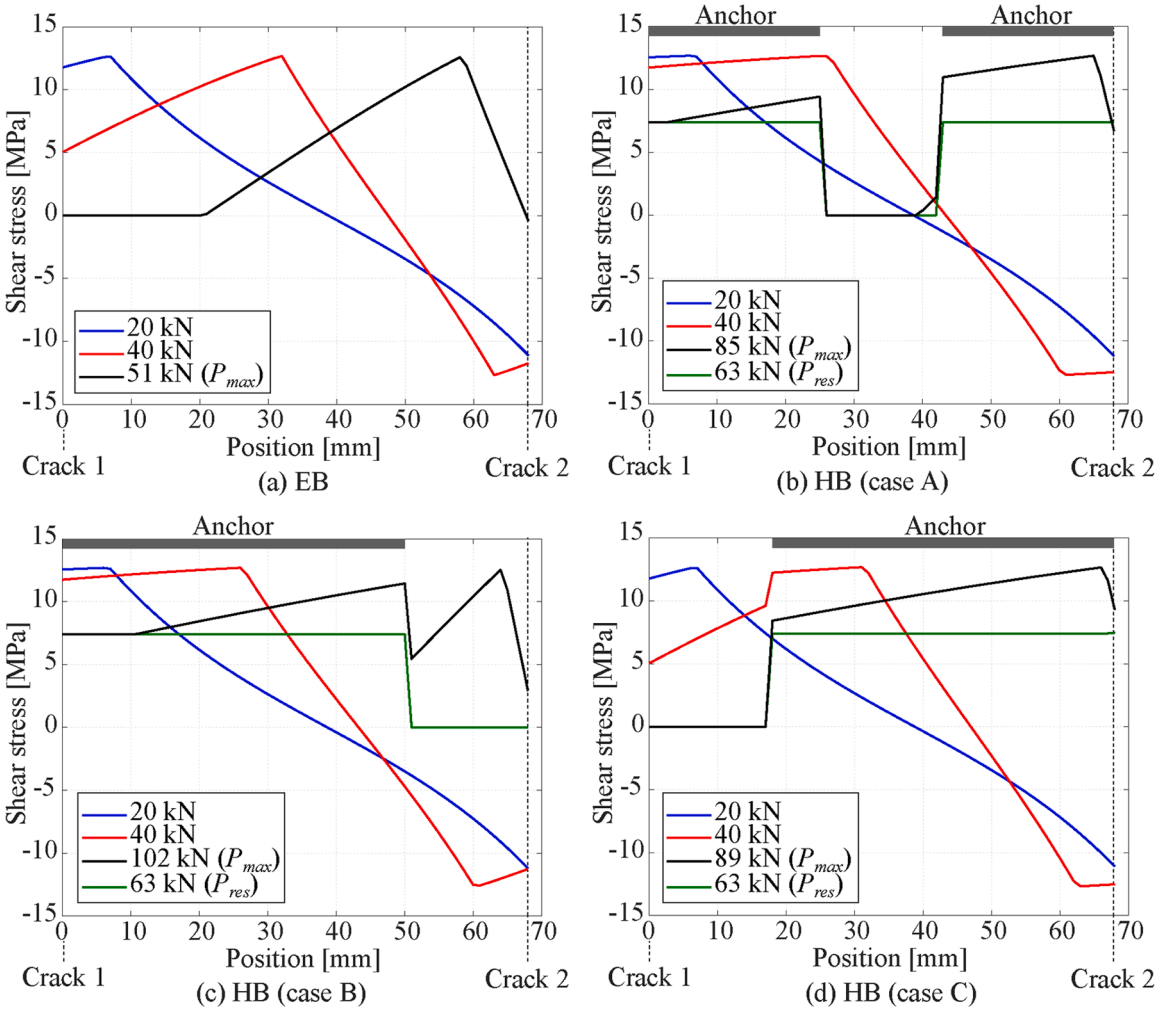

Fig. 15. Comparison of shear stress distributions for EB and HB specimens with different anchor positions, with $s_r = 68$ mm and $\alpha = 0.7$.

the lower loaded end of the anchor (position = 68 mm), debonding occurs in the unanchored zone (position = 25–43 mm for case A, position = 18–68 mm for case C). While in case A part of the anchor is already under residual stresses after debonding in the higher loaded end zone (position = 0–25 mm), in case C the whole anchor remains in the softening branch of the shear stress-slip curve, contributing to a higher load capacity (position = 18–68 mm).

Based on the obtained results, in the subsequent application of the model, the cracks will be located at the midpoint of the anchor (as in case A) when considering an average crack spacing, being this the most conservative option in terms of bond capacity when $\alpha = 0.7$.

5.3. Application of the numerical model to the tested beams

In order to predict the failure load caused by ICD in the tested beams, it is necessary to compare the increase in tensile forces within the FRP of each concrete element between cracks, induced by bending stresses, with the bond capacity of that element calculated using the proposed model. The process begins with the determination of the position of the cracks, followed by establishing the FRP tensile forces at each crack position through the equilibrium of forces and deformations. Employing an iterative procedure, the FRP tensile force at the higher loaded end of each concrete element between cracks is compared to the corresponding value predicted by the bonded joint model (Fig. 12b), considering identical geometrical and loading configurations. This iterative step is repeated until failure is observed. More details of the procedure can be found in Ref. [40].

To assess the sensitivity of the predicted ICD failure load concerning crack spacing, different situations were analysed. These include the actual experimental position of the cracks illustrated in Fig. 9 ($s_{r,failure}$) and the experimental average crack spacing ($s_{r,avg}$). As previously mentioned, for HB specimens, a crack at each anchor midpoint was considered more appropriate. For the sake of simplicity, $s_{r,avg}$ for HB specimens was rounded to the nearest integer value, resulting in the crack spacing values reported in Table 7. This adjustment had no significant effect on the outcomes of the numerical model. Results, presented in Table 7 in relation to the maximum load before ICD under different crack spacing values, show that the proposed model consistently provides accurate predictions of the failure load for both EB and HB techniques when employing the experimental position of the cracks ($s_{r,failure}$). The ratio between theoretical and experimental loads falls within the range of 1.00–1.06. It is worth noting that, in all cases, the element that theoretically failed is positioned near the load application point, where the highest increment of forces occurred.

Upon comparing these results with predictions obtained using the average experimental crack spacing ($s_{r,avg}$), minimal differences were observed, with ratios between theoretical and experimental loads ranging from 0.97 to 1.03. This observation is valuable as adopting a constant s_r value substantially reduces the computational efforts involved in the analysis.

Table 7
Prediction of ICD failure using the proposed model with experimental and theoretical values of s_r.

Specimen label	$s_{r,failure}$			$s_{r,avg}$		
	s_r (mm)	$P_{max,th}$ (kN)	$P_{max,th}/P_{max,exp}$	s_r (mm)	$P_{max,th}$ (kN)	$P_{max,th}/P_{max,exp}$
EB	See Fig. 9	53.32	1.00	68	51.39	0.97
HB-S300		61.11	1.06	60	59.50	1.03
HB-S100		69.79[1]	1.01	50	69.79[1]	1.03

[1] Load due to concrete crushing failure. ICD does not take place according to the proposed model.

6. Conclusions

An experimental campaign including RC beams and single-shear tests strengthened with CFRP laminates through EB and HB-FRP techniques was carried out. In the HB-FRP strengthened RC beams, two anchor spacings were examined. In the single-shear experiments, three different bonding configurations were investigated: EB, HB in which one anchor was placed in the middle of the EB bonded length, and HB in which only the EB part under the anchor was bonded onto the concrete. A numerical methodology for predicting ICD failure in RC beams externally strengthened with CFRP laminates was developed. Using the finite differences method, this approach allowed for the implementation of different bond-slip laws at different positions. Consequently, it is applicable to the HB-FRP technique, allowing the inclusion of the calibrated bond-slip laws for both EB-FRP and anchors at their corresponding positions. From this study, the following conclusions can be drawn:

1. HB-FRP increased the bond and flexural capacity of the specimens with EB-FRP by adding a residual strength after debonding of the FRP laminate. Additionally, the flexural capacity of the beams improved when reducing the anchor spacing.
2. In the single-shear tests, introducing one anchor to the EB-FRP specimen with a torque of 10 Nm led to a 35 % increase in bond capacity. After microcracking of the EB-concrete interface, the anchor became active, significantly increasing the load capacity until complete debonding.
3. The HB-FRP flexural RC specimens exhibited increased bending capacity compared to EB-FRP ones, with an 8 % increase in load capacity for specimen HB-S300 (anchor spacing = 300 mm) and a 27 % for HB-S100 (anchor spacing = 100 mm). The reduction in anchor spacing from 300 mm to 100 mm effectively limited debonding in localised sections, allowing the load to increase until failure occurred due to concrete crushing, while in EB and HB-S300 beams failure was attributed to ICD. Additionally, the HB technique led to a more efficient use of the CFRP laminate, resulting in higher strain values, which increased by a 17 % in HB-300 and a 95 % in HB-S100.
4. The introduction of anchors favoured the appearance of cracks, resulting in at least one crack at each anchor. Reducing the crack spacing may also contribute to delaying ICD failure mode.
5. In the proposed model, the calculation of bond capacity for the concrete element between flexural cracks in different strengthening systems relies on three key parameters: the variation in tensile forces in the FRP at both sides of the element between cracks, the crack spacing, and the anchor position in the bonded joint. Based on obtained results, for the subsequent application of the model, placing the crack at the midpoint of the anchor is considered the most reasonable option.
6. The proposed model gave accurate results (ratio $P_{max,th}/P_{max,exp}$ within the range of 0.97–1.03) for EB and HB-CFRP RC beams considering the bond-slip laws obtained from the single-shear tests and the experimental values of the average crack spacing in the beams.
7. The study also investigated the impact of crack spacing in the proposed model. Minimal differences were observed when employing a constant average crack spacing value compared to using the exact positions of the cracks, resulting in a range of values for the ratio of theoretical to experimental bending capacities ($P_{max,th}/P_{max,exp}$) of 0.97–1.03 versus 1.00–1.06, respectively.

Funding

This work was supported by the Spanish Ministry of Science and Innovation (MCIN/AEI) under project PID2020-119015GB-C22 (MCIN/AEI/10.13039/5011000011033) and the Generalitat de Catalunya, under the Grant number 2020_FISDU 00476.

Declaration of Competing Interest

The authors declare the following financial interests/personal relationships which may be considered as potential competing interests: Alba Codina reports financial support was provided by Ministerio de Ciencia e Innovación (ES). Alba Codina reports financial support was provided by Agència de Gestió d'Ajuts Universitaris i de Recerca (ES). The co-author Cristina Barris is an editor of the Construction and Building Materials journal. If there are other authors, they declare that they have no known competing financial interests or personal relationships that could have appeared to influence the work reported in this paper.

Acknowledgements

The authors wish to acknowledge the support of S&P Clever Reinforcement Ibérica Lda. for supplying the laminates and the epoxy resin used in this study.

Data availability

Data will be made available on request.

References

[1] C.E. Bakis, L.C. Bank, F. Asce, V.L. Brown, M. Asce, E. Cosenza, et al., Fiber-reinforced polymer composites for construction-state-of-the-art review, J. Compos. Constr. 6 (2002) 73–87, https://doi.org/10.1061/ASCE1090-026820026:273.
[2] A. Siddika, M.A. Mamun, Al, R. Alyousef, Y.H.M. Amran, Strengthening of reinforced concrete beams by using fiber-reinforced polymer composites: a review, J. Build. Eng. 25 (2019) 100798, https://doi.org/10.1016/J.JOBE.2019.100798.
[3] C. Mazzotti, A. Bilotta, C. Carloni, F. Ceroni, T. D'Antino, E. Nigro, , 2016, Bond between EBR FRP and Concrete. RILEM State-of-the-Art Reports, vol. 19, Springer Netherlands; 2016, p. 39–96. https://doi.org/10.1007/978-94-017-7336-2_3.
[4] E. Oller, D. Cobo, A.R. Marí, Design proposal to avoid peeling failure in FRP-strengthened reinforced concrete beams, J. Compos. Constr. 13 (2009) 384–393, https://doi.org/10.1061/(asce)cc.1943-5614.0000038.
[5] ACI Committee 440. ACI 440.2R-17: Guide for the design and construction of externally bonded FRP systems for strengthening concrete structures. Farmington Hills, Michigan, USA: American Concrete Institute (ACI), 2017.
[6] Fib Task Group 5.1. fib bulletin 90: Externally applied FRP reinforcement for concrete structures. Lausanne, Switzerland: Task Group 5.1 "Fibre-Reinforced Polymer Reinforcement for concrete structures", 2019.
[7] Consiglio Nazionalle delle Richerche (CNR). CNR-DT 200 R1/2013: Guide for the Design and Construction of Externally Guide for the Design and Construction of Externally Bonded FRP Systems for Strengthening Existing Structures. Rome, Italy: Consiglio Nazionalle delle Richerche (CNR), 2013.
[8] A. Codina, C. Barris, Y. Jahani, M. Baena, L. Torres, Assessment of fib Bulletin 90 design provisions for intermediate crack debonding in flexural concrete elements strengthened with externally bonded FRP, Polymers (Basel) 15 (2023), https://doi.org/10.3390/polym15030769.
[9] R. Kalfat, J. Gadd, R. Al-Mahaidi, S.T. Smith, An efficiency framework for anchorage devices used to enhance the performance of FRP strengthened RC members, Constr. Build. Mater. 191 (2018) 354–375, https://doi.org/10.1016/J.CONBUILDMAT.2018.10.022.
[10] R. Kalfat, R. Al-Mahaidi, S.T. Smith, Anchorage devices used to improve the performance of reinforced concrete beams retrofitted with FRP composites: state-of-the-art review, J. Compos. Constr. 17 (2013) 14–33, https://doi.org/10.1061/(asce)cc.1943-5614.0000276.
[11] Y.-F. Wu, Y. Huang, Hybrid bonding of FRP to reinforced concrete structures, J. Compos. Constr. 12 (2008), https://doi.org/10.1061/(asce)1090-0268(2008)12:3(266).
[12] C. Chen, L. Sui, F. Xing, D. Li, Y. Zhou, P. Li, Predicting bond behavior of HB FRP strengthened concrete structures subjected to different confining effects, Compos Struct. 187 (2018) 212–225, https://doi.org/10.1016/j.compstruct.2017.12.036.
[13] L. Gao, F. Zhang, J. Liu, X. Lu, H. Gao, Experimental and numerical study on the interfacial bonding characteristics of FRP-to-concrete joints with mechanical fastening, Constr. Build. Mater. 199 (2019) 456–470, https://doi.org/10.1016/J.CONBUILDMAT.2018.12.033.
[14] Y.-F. Wu, K. Liu, Characterization of mechanically enhanced FRP bonding system, J. Compos. Constr. 17 (2013) 34–49, https://doi.org/10.1061/(ASCE)CC.1943-5614.0000302.
[15] Y. Zhou, X. Wang, L. Sui, F. Xing, Z. Huang, C. Chen, et al., Effect of mechanical fastening pressure on the bond behaviors of hybrid-bonded FRP to concrete interface, Compos. Struct. 204 (2018) 731–744, https://doi.org/10.1016/j.compstruct.2018.08.008.
[16] X.H. Gao, L. Gao, F. Zhang, A new bond-slip model of hybrid bonded FRP-to-concrete joints, KSCE J. Civ. Eng. 27 (2023) 270–284, https://doi.org/10.1007/s12205-022-2286-4.
[17] F. Zhang, L. Gao, Q. Wei, Theoretical and numerical bonding capacity model of FRP-to-concrete joints with mechanical fastening, Constr. Build. Mater. 353 (2022), https://doi.org/10.1016/j.conbuildmat.2022.129066.
[18] J.G. Teng, H. Yuan, J.F. Chen, FRP-to-concrete interfaces between two adjacent cracks: theoretical model for debonding failure, Int. J. Solids Struct. 43 (2006) 5750–5778, https://doi.org/10.1016/j.ijsolstr.2005.07.023.
[19] J.F. Chen, H. Yuan, J.G. Teng, Debonding failure along a softening FRP-to-concrete interface between two adjacent cracks in concrete members, Eng. Struct. 29 (2007) 259–270, https://doi.org/10.1016/j.engstruct.2006.04.017.
[20] C. Chen, X. Wang, L. Sui, F. Xing, X. Chen, Y. Zhou, Influence of FRP thickness and confining effect on flexural performance of HB-strengthened RC beams, Compos. B Eng. 161 (2019) 55–67, https://doi.org/10.1016/j.compositesb.2018.10.059.
[21] F. Zhang, L. Gao, L. Zhang, Numerical simulation and flexural capacity of hybrid-bonded FRP reinforced concrete beam, Arab. J. Sci. Eng. 48 (2023) 12845–12858, https://doi.org/10.1007/s13369-022-07587-7.
[22] F. Zhang, L. Gao, Y.F. Wu, J. Liu, Flexural design of reinforced concrete structures strengthened with hybrid bonded FRP, Compos. Struct. 269 (2021) 113996, https://doi.org/10.1016/J.COMPSTRUCT.2021.113996.
[23] Y.F. Wu, J.H. Yan, Y.W. Zhou, Y. Xiao, Ultimate strength of reinforced concrete beams retrofitted with hybrid bonded fiber-reinforced polymer, Acids Struct. J. 107 (2010), https://doi.org/10.14359/51663818.
[24] L. Gao, Q. Wei, Y. Huang, F. Zhang, Influence of anchor design parameters on flexural performance of hybrid bonded-fiber reinforced polymer strengthened reinforced concrete beams, Structures 48 (2023) 1029–1045, https://doi.org/10.1016/j.istruc.2023.01.025.
[25] Z.M. Wu, C.H. Hu, Y.F. Wu, J.J. Zheng, Application of improved hybrid bonded FRP technique to FRP debonding prevention, Constr. Build. Mater. 25 (2011) 2898–2905, https://doi.org/10.1016/j.conbuildmat.2010.12.033.
[26] UNE-EN 12390-3, Testing Hardened Concrete - Part 3: Compressive Strength of Test Specimens, AENOR, Madrid, 2011.
[27] UNE-EN 12390-6, Testing Hardened Concrete - Part 6: Tensile Splitting Strength of Test Specimens, AENOR, Madrid, 2010.
[28] ASTM C469/C469M-10. Standard Test Method for Static Modulus of Elasticity and Poisson's Ratio of Concrete in Compression. West Conshohocken, PA, USA: 2010.
[29] UNE-EN ISO 15630-1. Steel for the Reinforcement and Prestressing of Concrete-Test Methods - Part 1: Reinforcing Bars, Wire Rod and Wire. AENOR: Madrid: 2011.
[30] I. Iovinella, A. Prota, C. Mazzotti, Influence of surface roughness on the bond of FRP laminates to concrete, Constr. Build. Mater. 40 (2013) 533–542, https://doi.org/10.1016/j.conbuildmat.2012.09.112.
[31] Finckh W., Niedermeier R., Zilch K. Praxisgerechte Bemessungsansätze für das wirtschaftliche Verstärken von Betonbauteilen mit geklebter Bewehrung - Verbundtragfähigkeit unter statischer Belastung. In: Beuth, editor. DAfStb Heft 592, Berlin: 2012.
[32] J.F. Chen, J.G. Teng, Anchorage strength models for FRP and steel plates bonded to concrete, J. Struct. Eng. 127 (2001) 784–791.
[33] A. Bilotta, F. Ceroni, E. Nigro, M. Pecce, Design by testing of debonding load in RC elements strengthened with EBR FRP materials, Am. Concr. Inst. Acids Spec. Publ. 1 (2011) 463–482.
[34] C. Mazzotti, M. Savoia, B. Ferracuti, A new single-shear set-up for stable debonding of FRP-concrete joints, Constr. Build. Mater. 23 (2009) 1529–1537, https://doi.org/10.1016/j.conbuildmat.2008.04.003.
[35] M.A. Al-Saawani, A.K. El-Sayed, A.I. Al-Negheimish, Effect of shear-span/depth ratio on debonding failures of FRP-strengthened RC beams, J. Build. Eng. 32 (2020) 101771, https://doi.org/10.1016/J.JOBE.2020.101771.
[36] K. Zilch, R. Niedermeier, W. Finckh. Strengthening of Concrete Structures with Adhesively Bonded Reinforcement, Ernst & Sohn, 2014, 10.1002/9783433604014.
[37] J. Gómez, L. Torres, C. Barris, Characterization and simulation of the bond response of NSM FRP reinforcement in concrete, Materials 13 (2020), https://doi.org/10.3390/MA13071770.
[38] L. Gao, F. Zhang, J.-Q. Liu, X.-R. Lu, Whole-process bond characteristics of FRP-to-concrete joint under pressure, KSCE J. Civ. Eng. 22 (2018) 5114–5122, https://doi.org/10.1007/s12205-018-0177-5.
[39] F. Ceroni, J.A.O. Barros, M. Pecce, M. Ianniciello, Assessment of nonlinear bond laws for near-surface-mounted systems in concrete elements, Compos. B Eng. 45 (2013) 666–681, https://doi.org/10.1016/j.compositesb.2012.07.006.
[40] A. Codina, C. Barris, Y. Jahani, M. Baena, L. Torres, Experimental and theoretical study on the flexural behaviour of RC beams strengthened with externally bonded reinforcement on grooves CFRP laminates, Eng. Struct. 299 (2024), https://doi.org/10.1016/j.engstruct.2023.117091.